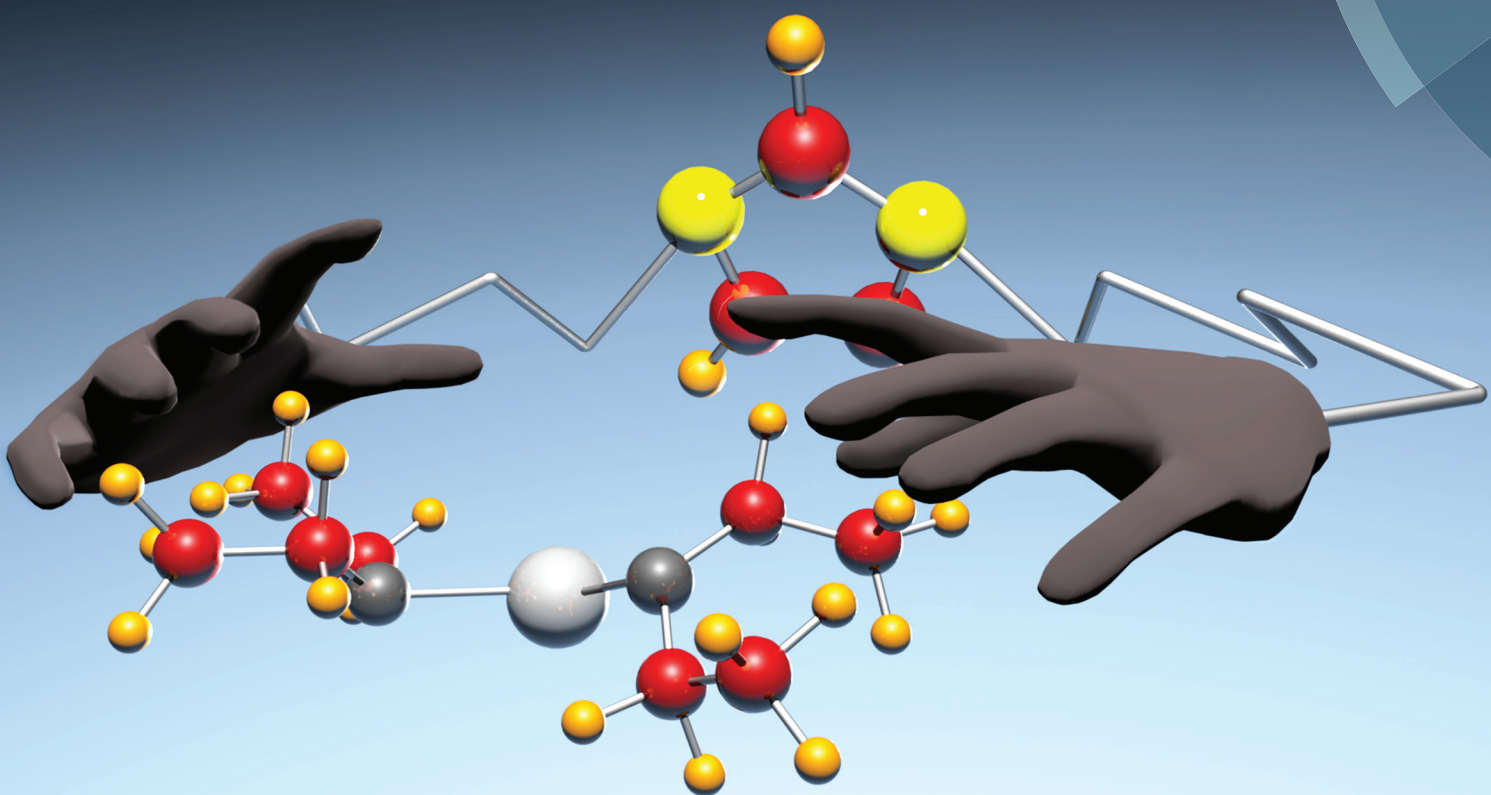


# Dalton Transactions

An international journal of inorganic chemistry

[rsc.li/dalton](http://rsc.li/dalton)



ISSN 1477-9226



PAPER

Anja Mudring, Stephan Schulz, Gabi Schierning *et al.*  
Improving the  $zT$  value of thermoelectrics by nanostructuring: tuning the nanoparticle morphology of  $\text{Sb}_2\text{Te}_3$  by using ionic liquids



Cite this: *Dalton Trans.*, 2017, **46**, 656

## Improving the $zT$ value of thermoelectrics by nanostructuring: tuning the nanoparticle morphology of $\text{Sb}_2\text{Te}_3$ by using ionic liquids

Julian Schaumann,<sup>a,b</sup> Manuel Loor,<sup>a,b</sup> Derya Ünal,<sup>a</sup> Anja Mudring,<sup>\*a,c</sup> Stefan Heimann,<sup>b</sup> Ulrich Hagemann,<sup>d</sup> Stephan Schulz,<sup>\*b</sup> Franziska Maculewicz<sup>e</sup> and Gabi Schierning<sup>\*e,f</sup>

A systematic study on the microwave-assisted thermolysis of the single source precursor  $(\text{Et}_2\text{Sb})_2\text{Te}$  (**1**) in different asymmetric 1-alkyl-3-methylimidazolium- and symmetric 1,3-dialkylimidazolium-based ionic liquids (ILs) reveals the distinctive role of both the anion and the cation in tuning the morphology and microstructure of the resulting  $\text{Sb}_2\text{Te}_3$  nanoparticles as evidenced by X-ray diffraction (XRD), scanning electron microscopy (SEM), energy dispersive X-ray analysis (EDX), and X-ray photoelectron spectroscopy (XPS). A comparison of the electrical and thermal conductivities as well as the Seebeck coefficient of the  $\text{Sb}_2\text{Te}_3$  nanoparticles obtained from different ILs reveals the strong influence of the specific IL, from which  $\text{C}_4\text{miml}$  was identified as the best solvent, on the thermoelectric properties of as-prepared nano-sized  $\text{Sb}_2\text{Te}_3$ . This work provides design guidelines for ILs, which allow the synthesis of nanostructured thermoelectrics with improved performances.

Received 14th November 2016,  
Accepted 22nd December 2016

DOI: 10.1039/c6dt04323b  
[www.rsc.org/dalton](http://www.rsc.org/dalton)

## Introduction

Thermoelectric generators (TEG) directly convert heat fluxes into useable electrical energy and therefore provide a wear- and noiseless power source.<sup>1</sup> The efficiency of a thermoelectric material is defined by the dimensionless figure of merit  $zT$  ( $(\alpha^2\sigma/\kappa)T$ ), where  $\alpha$  is the Seebeck coefficient,  $\sigma$  the specific electrical conductivity,  $\kappa$  the thermal conductivity as the sum of the electronic  $\kappa_{\text{el}}$  and the lattice  $\kappa_{\text{L}}$  contribution and  $T$  the absolute temperature in Kelvin. It is assumed that at least a  $zT \geq 1.5$  is necessary for most technical applications to become efficient and commercially viable.<sup>2</sup> Unfortunately, the electrical and thermal transport coefficients are interrelated and cannot easily be optimized independently from each other. Metals naturally show high electrical and thermal con-

ductivities, whereas both of these are small for insulators such as ceramics. The best choices of materials for technical applications in thermoelectric devices are semiconducting materials which contain heavy elements. This inherently minimizes the thermal conductivity due to a low speed of sound of such materials, while still a sufficiently high electronic conductivity is obtained. For technical applications near room temperature,  $\text{Sb}_2\text{Te}_3$  and  $\text{Bi}_2\text{Te}_3$  as well as their solid ternary solutions  $(\text{Sb}_x\text{Bi}_{1-x})_2\text{Te}_3$  are currently the most efficient materials due to their high electrical conductivities and high Seebeck coefficients combined with low thermal conductivities.<sup>3</sup>

$\text{Sb}_2\text{Te}_3$  is a tetradymite-type layered material, which has been investigated for decades since it is a narrow band-gap ( $E_{\text{gap}} 0.26$  eV) semiconductor with good thermoelectric characteristics near room temperature.<sup>4</sup> More recently, interest in  $\text{Sb}_2\text{Te}_3$  increased due to its capability to serve as a topological insulator.<sup>5</sup> Nanostructuring has been demonstrated theoretically and experimentally to greatly improve the figure of merit by effectively reducing the lattice contribution to the thermal conductivity<sup>6</sup> while the electrical conductivity of the material is mostly unaffected. Different types of scattering centres for the heat carrying phonons such as nanoscale precipitates or grain boundaries and other interfaces have been employed for optimizing thermoelectric materials this way.<sup>7</sup> Even a hierarchical design of the nano- and microstructure was developed to effectively scatter the

<sup>a</sup>Inorganic Chemistry III – Materials Synthesis and Characterization, Ruhr-Universität Bochum, DE-44801 Bochum, Germany. E-mail: mudring@iastate.edu

<sup>b</sup>Faculty of Chemistry and Center for NanoIntegration (CENIDE), University of Duisburg-Essen, DE-45117 Essen, Germany. E-mail: stephan.schulz@uni-due.de

<sup>c</sup>Department of Materials Science and Engineering, Iowa State University and Ames Laboratory, U.S. Department of Energy, Ames, IA 50011, USA

<sup>d</sup>Interdisciplinary Center for Analytics on the Nanoscale (ICAN), NETZ, University of Duisburg-Essen, Carl-Benz-Str. 199, 47047 Duisburg, Germany

<sup>e</sup>Faculty of Engineering and Center for NanoIntegration (CENIDE),

University of Duisburg-Essen, Bismarckstr. 81, DE-47057 Duisburg, Germany

<sup>f</sup>Institute for Metallic Materials, IFW Dresden, P.O. Box 270116, D-01171 Dresden, Germany. E-mail: g.schierning@ifw-dresden.de



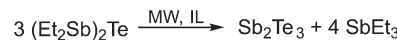
broad spectrum of phonon wavelengths, which led to record-high  $zT$  values.<sup>8</sup>

Our general interest in thermoelectric materials prompted us to investigate the synthesis of binary ( $\text{Sb}_2\text{Te}_3$ ,  $\text{Bi}_2\text{Te}_3$ ) and ternary ( $[\text{Sb}_x\text{Bi}_{1-x}]_2\text{Te}_3$ ) materials both in solution<sup>9</sup> and *via* gas phase based processes such as atomic layer deposition (ALD)<sup>10</sup> and metal organic chemical vapour deposition (MOCVD)<sup>11</sup> using single-source and dual-source precursor approaches. The microwave-assisted decomposition of the single source precursor ( $\text{Et}_2\text{Sb})_2\text{Te}$  **1** in an ionic liquid (IL) had been shown to produce highly stoichiometric  $\text{Sb}_2\text{Te}_3$  nanoparticles,<sup>12a</sup> while  $\text{Bi}_2\text{Se}_3$ ,  $\text{Bi}_2\text{Te}_3$  and  $(\text{Sb}_x\text{Bi}_{1-x})_2\text{Te}_3$  nanoparticles were synthesized by using specific reactive ILs.<sup>12b,c</sup> The  $\text{Sb}_2\text{Te}_3$  nanoparticles showed exceptionally high figures of merit of up to 1.5 at 300 °C, without the need of alloying or electronic doping. This new synthetic strategy allowed an effective decoupling of electronic and phononic transport properties.<sup>12a</sup> In our studies we made the observation that the  $\text{Sb}_2\text{Te}_3$  particle morphology changed depending on the chemical identity of the ionic liquids, which prompted us to study their influence on the microwave-assisted decomposition of **1** in more detail and look for correlations with the thermal and electronic transport properties in the obtained material.

We herein report on our systematic study on the decomposition of **1** in different ILs, in which both the anion and the cation were systematically varied, using microwave-assisted techniques. In addition, the results from detailed transport measurement of the resulting  $\text{Sb}_2\text{Te}_3$  nanoparticles are reported that allow for a structure–property analysis.

## Results and discussion

We have recently developed a synthetic protocol that enabled us to access  $\text{Sb}_2\text{Te}_3$  nanomaterials with a record-figure of merit by the decomposition of **1** in the ionic liquid  $\text{C}_4\text{mimBr}$  ( $\text{C}_4\text{mim}$  = 1-butyl-3-methylimidazolium) under microwave (MW) irradiation.<sup>12a</sup> As the IL acted in this reaction not only as the solvent but also as the heat transfer medium, we herein study the specific role of the IL as the nanotemplating agent by investigating a set of ILs based on 1,3-dialkylimidazolium cations. Starting from the most prominent IL cation, 1-butyl-3-methylimidazolium ( $\text{C}_4\text{mim}^+$ ), first the counter anion was varied from  $\text{Cl}^-$ ,  $\text{Br}^-$ ,  $\text{I}^-$  to  $\text{NTf}_2^-$  ( $\text{NTf}_2^-$  = bis(trifluoromethane-sulfonyl)amide). Variation of the IL anion not only leads to a change in fundamental physical properties of the IL such as the melting point or viscosity but also its solvation properties such as polarity. Moreover, the chosen anions range from relatively strongly coordinating ( $\text{Cl}^-$ ) to quite weakly coordinating ( $\text{NTf}_2^-$ ) anions. In the context of nanomaterial synthesis the capabilities of the IL ions to interact with the as-formed nuclei and crystal seeds is especially important as this allows for the morphology<sup>13</sup> and even the phase control<sup>14</sup> of nanomaterials. The Lewis basicity of these ILs decreased in the order of  $\text{Cl}^-$ ,  $\text{Br}^-$ ,  $\text{I}^-$  to  $\text{NTf}_2^-$ .<sup>15</sup> Similarly, variations of the cation influence the overall IL properties.



**Scheme 1** Synthesis of  $\text{Sb}_2\text{Te}_3$  nanoparticles by microwave-assisted decomposition of the single source precursor **1**.

Generally an increase of the melting point with increasing chain length of the alkyl group is observed for imidazolium based ILs. Symmetrically substituted imidazolium ILs typically exhibit higher melting points than asymmetrical ILs.<sup>16</sup> Again, in the context of tuning the nanostructure of a material through the templating effect of the IL, the interaction of the IL cation with the nanomaterial needs to be considered. Imidazolium cations can interact not only electrostatically, but, as they bear acidic protons (the 2H proton of the imidazolium ring is especially acidic) and an aromatic  $\pi$ -system, can also undergo secondary bonding interactions such as hydrogen bonding and  $\pi$ -bonding. This has been found especially important in the synthesis of nanosized oxide materials.<sup>17</sup> However, the cation size can critically influence these bonding capabilities.<sup>18</sup> For this reason, the alkyl-chain of the  $\text{C}_4 \times \text{C}_1\text{mim}^+$  imidazolium cation was varied from three to eight carbon atoms.

In addition to the set of 1-methyl-*n*-alkylimidazolium bromides, the corresponding set of symmetrically substituted cations ( $\text{C}_n\text{C}_n\text{mim}^+$ ) with  $n = 4, 6$  and  $8$  were explored. Ionic liquids are known to be highly structured solvents,<sup>19</sup> which can impact nanoparticle formation critically.<sup>20</sup> In particular, for imidazolium cations with longer alkyl chains a highly ordered structure of the IL can be expected,<sup>21</sup> *i.e.* imidazolium-based ILs with more than eleven carbon atoms in the side chain tend to form thermotropic liquid crystalline phases. The use of ordered phases as the template in nanoparticle synthesis has already been reported.<sup>22</sup>

To obtain  $\text{Sb}_2\text{Te}_3$  nanoparticles from various ionic liquids, in a typical reaction, **1** was added to the respective IL at 90 °C and stirred for 5 min until a homogeneous dispersion or solution was formed, which was then heated in a laboratory microwave oven first for 30 s at 100 °C, then for 5 s at 150 °C and finally for 5 min at 170 °C. The resulting colloidal solution was centrifuged (2000 rpm), washed with 10 mL of acetonitrile (7×) to completely remove the by-product  $\text{SbEt}_3$  (Scheme 1) and dried at ambient temperature under reduced pressure. Black precipitates were obtained, which were characterized by powder X-ray diffraction (PXRD), energy dispersive X-ray analysis (EDX), scanning electron microscopy (SEM) and X-ray photoelectron spectroscopy (XPS).

### General product characterization

PXRD measurements confirmed the formation of phase-pure  $\text{Sb}_2\text{Te}_3$  in all ILs (see Fig. 1 for a representative PXRD pattern). All observed diffraction peaks can be indexed to the database pattern of  $\text{Sb}_2\text{Te}_3$  (JCPDS file 015874) and the lattice parameters were refined to  $a = 4.266(9)$  Å and  $c = 30.456(6)$  Å.

A small texture effect was observed since the intensity of the 1010 reflex was somewhat smaller compared to the



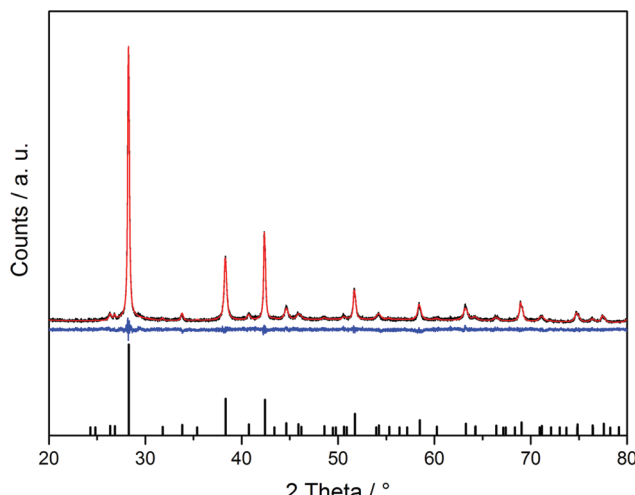


Fig. 1 Representative powder X-ray diffraction pattern of  $\text{Sb}_2\text{Te}_3$  nanoparticles (with  $\text{Cu K}\alpha$  radiation) including Rietveld refinements.

reference. Our samples show an intensity ratio of the 015 (28.3°):1010 (38.5°):110 (42.5°) reflex of 1:0.26:0.35, whereas this ratio in the reference was 1:0.35:0.33. A size determination of the nanoparticles typically yielded sizes of >300 nm, but these values should be taken with care due to their plate-like structure (see Fig. 4 and 5).

EDX analysis confirmed within standard deviations the stoichiometric composition of the products. In addition, no signals originating from the IL or contaminations, *i.e.* oxidation or hydrolysis products, were detected. These results were confirmed by infrared (IR) spectroscopy, showing no absorption band of the respective ILs on the particle surface. In contrast, the nanoparticles were shown to be partially oxidized at the surface by XPS, which is a much more surface sensitive analytical method compared to EDX and IR. Fig. 2 exemplarily shows the XPS spectra of  $\text{Sb}_2\text{Te}_3$  nanoparticles prepared in  $\text{C}_4\text{mimI}$ , while Fig. 3 displays XPS spectra of a sample obtained in  $\text{C}_4\text{mimNTf}_2$ .

The XPS spectra of the sample prepared in  $\text{C}_4\text{mimI}$  (Fig. 2) and  $\text{C}_4\text{mimNTf}_2$  (Te and Sb spectra at the top right and bottom right in Fig. 3) clearly showed that both Sb and Te are partially oxidized, as is clearly visible from the metal oxide peaks at 530.1 eV binding energy for the Sb 3d<sub>5/2</sub> and at 575.9 eV for the Te 3d<sub>5/2</sub> peaks. These findings are in good

agreement with the literature values.<sup>12b,c,23,24</sup> However, while only around 3% of the Te are present as an oxide in the case of Sb roughly 40% (prepared in  $\text{C}_4\text{mimI}$ ) to 60% (prepared in  $\text{C}_4\text{mimNTf}_2$ ) of the Sb is oxidized. The ratio of elemental Sb to elemental Te gives exactly the expected ratio of 2:3. This means that there is an excess of Sb at the surface and that this Sb is present as an oxide. Comparable surface oxidation reactions have been very recently observed for binary and ternary bismuth chalcogenide nanoparticles, in which  $\text{Bi}_2\text{Te}_3$  and  $\text{Bi}_2\text{Te}_2\text{Se}$  were found to easily oxidize upon exposure to air while  $\text{Bi}_2\text{Se}_3$  was significantly more stable toward oxidation.<sup>12b,c,31</sup> In addition,  $\text{Sb}_2\text{Te}_3$  thin films were found to be easily oxidized after exposure to atmosphere and a post-deposition treatment was therefore suggested by the authors as an effective method to promote the formation of the Sb–Te bond and prevent oxidation of the thin film surface. As a consequence, the nanoparticles have to be stored and handled under inert gas conditions to avoid surface oxidation reactions. In addition, N, S, F, C and O (Fig. 3) are also found on the surface, which can be attributed to the residues of the ionic liquid ( $\text{C}_4\text{mimNTf}_2$ ) and the washing solvent ( $\text{CH}_3\text{CN}$ ), which can also coordinate to the nanoparticle surface.

### Morphology of $\text{Sb}_2\text{Te}_3$ nanoparticles synthesised in different ILs

*Role of the anion ( $An^-$ ) of 1-alkyl-3-methyl-imidazolium based ionic liquids  $\text{C}_4\text{mimAn}$ .* The role of the anion ( $\text{Cl}^-$ ,  $\text{Br}^-$ ,  $\text{I}^-$ ,  $\text{NTf}_2^-$ ) of the 1-butyl-3-methyl-imidazolium based ionic liquid in tuning the composition and the morphology of the resulting nanoparticles was investigated by SEM. All four samples show the formation of hexagonally shaped  $\text{Sb}_2\text{Te}_3$  nanoplates with diameters ranging between 300–2000 nm and varying in thickness between 65–120 nm (Fig. 4).

These platelets form larger agglomerates. Both the dimensions of the nanoplates and the type of agglomeration are strongly influenced by the IL anion. The thickness of the individual hexagonal platelets increased while changing the IL anion from  $\text{Cl}^-$ ,  $\text{Br}^-$ ,  $\text{I}^-$  to  $\text{NTf}_2^-$ . Also, the association of these platelets changed from individual sandrose-type spherical aggregates over more aggregated spheres of platelets to less spherical, less extended aggregates. This observation could be correlated with the coordination ability of the IL anion. Chloride is a strongly Lewis basic, coordinating anion whereas the  $\text{NTf}_2$  anion has a weak coordination ability. Thus, ionic liquids with rather strongly coordinating anions force the

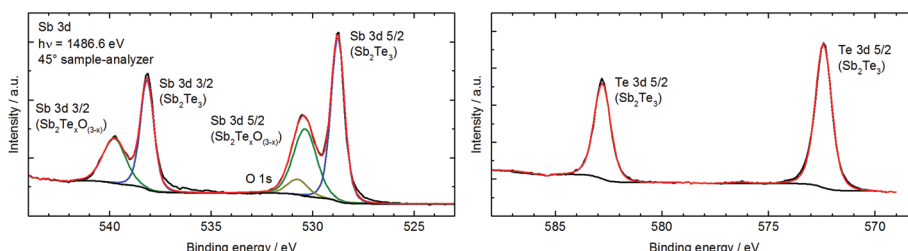


Fig. 2 Representative XPS spectra of  $\text{Sb}_2\text{Te}_3$  nanoparticles synthesized in  $\text{C}_4\text{mimI}$ .



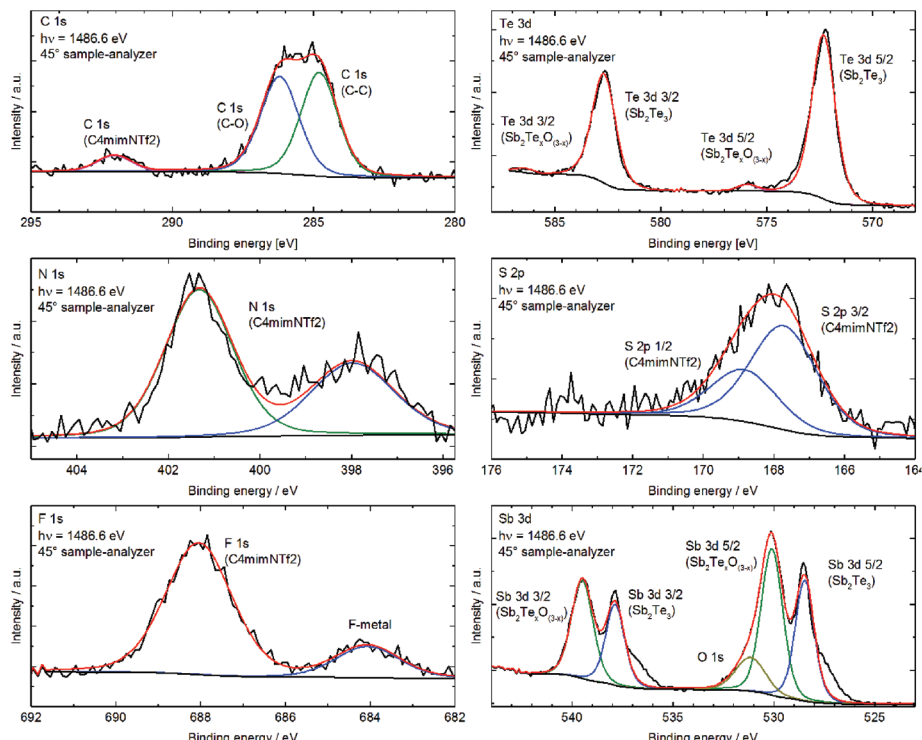


Fig. 3 Representative XPS spectra of  $\text{Sb}_2\text{Te}_3$  nanoparticles synthesized in  $\text{C}_4\text{mimNTf}_2$ .

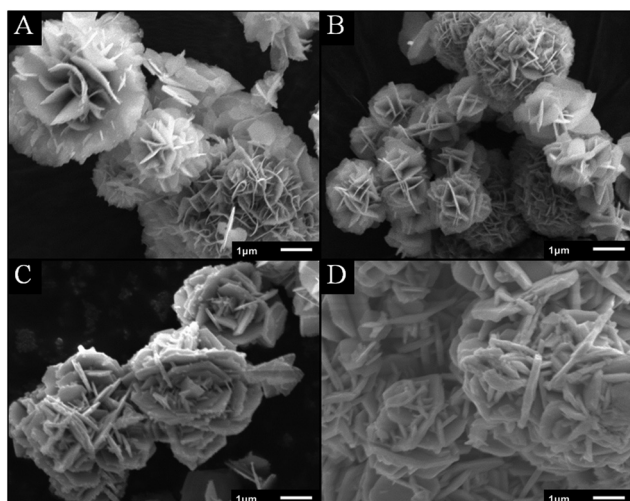


Fig. 4 SEM images of  $\text{Sb}_2\text{Te}_3$  nanoparticles synthesized in various ionic liquids. The nanoparticles in (A) were synthesized in  $\text{C}_4\text{mimCl}$ , (B) in  $\text{C}_4\text{mimBr}$ , (C) in  $\text{C}_4\text{mimI}$  and (D) in  $\text{C}_4\text{mimNTf}_2$ .

formation of thinner platelets as the vertical particle growth is hindered through the interaction of the IL anion with the particle surface. An IL with a less coordinating anion not only hinders the particle growth less, resulting in the formation of thicker platelets, but also stabilizes the particles less against further agglomeration and, in consequence, larger agglomerates are found in  $\text{C}_4\text{mimNTf}_2$ .

*Influence of the alkyl chain length of asymmetrical 1-n-alkyl-3-methylimidazolium bromide ionic liquids  $\text{C}_n\text{mimBr}$  ( $n = 3-8$ ).* To investigate the influence of the IL cation on the morphology of the  $\text{Sb}_2\text{Te}_3$  nanoparticles, a set of 1-n-alkyl-3-methylimidazolium bromides was synthesized and explored as the reaction medium in the synthesis of  $\text{Sb}_2\text{Te}_3$  nanoparticles through a microwave reaction.

The chain length of the 1-n-alkyl-3-methylimidazolium cation was systematically varied from three to eight carbon atoms. Bromide was chosen in these experiments as the anion in order to be comparable with the results of previous studies.<sup>12a</sup> In  $\text{C}_3\text{mimBr}$  exclusively isolated spherical aggregates of small platelets with diameters of 2–5  $\mu\text{m}$  were formed. By increasing the side chain length of the alkyl group of the 1-n-alkyl-3-methylimidazolium cation, the size and number of these aggregates shrink. At the same time individual larger hexagonal plates of  $\text{Sb}_2\text{Te}_3$  are formed, which have a smaller tendency to aggregate. When  $\text{C}_8\text{mimBr}$  is used in the synthesis, almost exclusively hexagonal plates are observed (Fig. 5).

It is obvious that the IL cation has a strong influence on the nanostructure of the obtained material and two factors appear to be important: *solubility* of the precursor in the IL and *structural order* of the IL. The solubility of the precursor increases with increasing alkyl-chain length of the cation, which can be correlated to the decreasing polarity of the IL. Whilst in ILs with short alkyl chains such as  $\text{C}_3\text{mimBr}$  and  $\text{C}_4\text{mimBr}$  only dispersions of  $(\text{Et}_2\text{Sb})_2\text{Te}$  in the IL were obtained, a full solubility of the precursor was observed for  $\text{C}_8\text{mimBr}$ . As a conse-

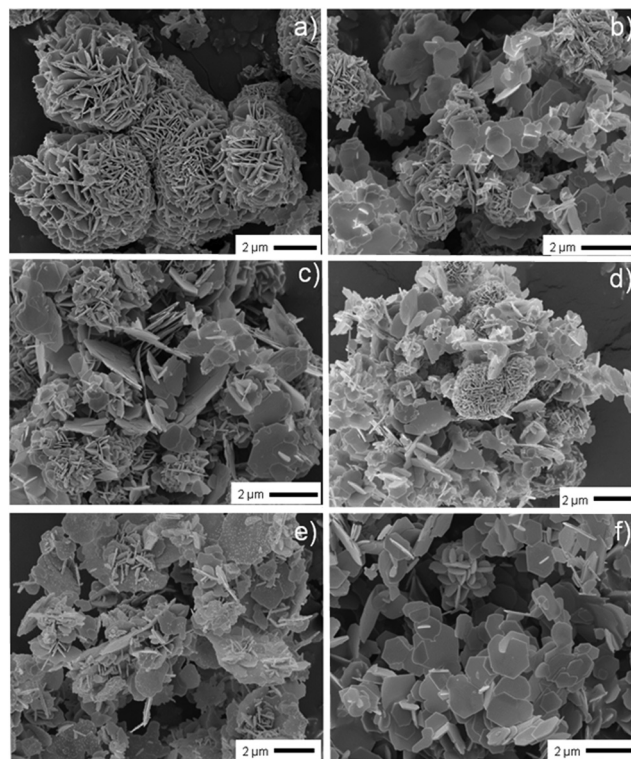


**Fig. 5** SEM images of  $\text{Sb}_2\text{Te}_3$  nanoparticles synthesized in 1-*n*-alkyl-3-methylimidazolium bromide  $\text{C}_n\text{C}_n\text{ImBr}$  with (a)  $n = 3$ , (b)  $n = 4$ , (c)  $n = 5$ , (d)  $n = 6$ , (e)  $n = 7$ , and (f)  $n = 8$ .

quence, the tendency of the formation of inhomogeneously distributed micro-drops of **1** in the IL increases with decreasing alkyl chain length of the IL, which obviously facilitates the formation of ball-like agglomerates upon thermolysis. In contrast, thermolysis of a homogeneous solution of **1** in the IL containing long alkyl chains leads to a steady growth of the  $\text{Sb}_2\text{Te}_3$  nanoparticles, which consequently form large sheets. In addition, it is known for 1-alkyl-3-methylimidazolium bromides that an increasing alkyl chain length of the cation leads to an increasing structural order, which may lead to the formation of lamellar, smectic liquid crystalline structures which could act as a template.<sup>21b,c</sup> Therefore, a set of symmetrically substituted 1-*n*-alkyl-3-*n*-alkylimidazolium bromides was tested as the reaction medium.

**Influence of the alkyl chain length of symmetrical 1,3-*n*-alkylimidazolium bromide ionic liquids  $\text{C}_n\text{C}_n\text{ImBr}$ .** The synthesis of  $\text{Sb}_2\text{Te}_3$  from **1** in  $\text{C}_n\text{C}_n\text{ImBr}$  with  $n = 4, 6$  and  $8$  yielded in all cases a phase pure material. However, while carrying out the synthesis in  $\text{C}_4\text{C}_4\text{ImBr}$ , only a dispersion of the single source precursor was obtained, whilst in  $\text{C}_6\text{C}_6\text{ImBr}$  and  $\text{C}_8\text{C}_8\text{ImBr}$  homogeneous solutions were formed (Fig. 6). The nanostructures of the material obtained from the different ILs show distinct differences. The trend in the change of the morphology, however, is similar to the observations made for asymmetrically substituted imidazolium bromides.

The nanoparticles synthesized in  $\text{C}_4\text{C}_4\text{ImBr}$  (Fig. 7A) consist of strongly agglomerated  $\text{Sb}_2\text{Te}_3$  nanoplates. Predominately

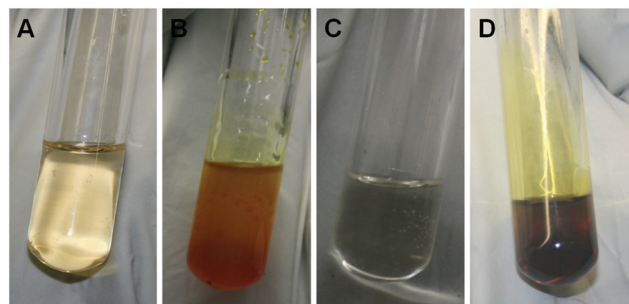


**Fig. 6** Pictures of neat  $\text{C}_4\text{C}_4\text{ImBr}$  (A),  $\text{C}_4\text{C}_4\text{ImBr} + \mathbf{1}$  (B), neat  $\text{C}_8\text{C}_8\text{ImBr}$  (C) and  $\text{C}_8\text{C}_8\text{ImBr} + \mathbf{1}$  (D).

sandrose-like structures with sizes between 1 and 4  $\mu\text{m}$  are formed by the aggregation of individual  $\text{Sb}_2\text{Te}_3$  particles, whose diameters range from 300 to 1200 nm. The diameter of the individual  $\text{Sb}_2\text{Te}_3$  platelets was found to increase with increasing alkyl-chain lengths of the IL cation. Individual nanoplates with diameters between 300 and 1500 nm were found in  $\text{C}_6\text{C}_6\text{ImBr}$  (Fig. 7B), while those obtained from  $\text{C}_8\text{C}_8\text{ImBr}$  (Fig. 7C) range from 300 to 2500 nm. In addition, the SEM images of the resulting nanoparticles clearly prove a decreasing agglomeration tendency of the hexagonal  $\text{Sb}_2\text{Te}_3$  nanoparticles with increasing chain length and hence increasing steric demand and coordination strength of the IL as were observed for the  $\text{Sb}_2\text{Te}_3$  nanoparticles obtained from unsymmetrical ILs (see Fig. 5). While compact ball-like agglomerates were formed with  $\text{C}_4\text{C}_4\text{ImBr}$ , the nanoparticles obtained in  $\text{C}_6\text{C}_6\text{ImBr}$  show loosely agglomerated card structures, and nanoparticles synthesized in  $\text{C}_8\text{C}_8\text{ImBr}$  consist of single  $\text{Sb}_2\text{Te}_3$  sheets and to some extent slightly crooked card structures (Fig. 7). With increasing alkyl chain length of the cation, the tendency of the formation of sandrose-like structures decreases. Instead, 3D agglomeration increases until finally in  $\text{C}_8\text{C}_8\text{ImBr}$  predominately large extended plates are formed. This confirms that an interplay of the precursor solubility and microstructure and the coordination ability of the IL strongly influence the microstructure formation.

Whenever the single source precursor **1** has poor solubility in the IL, sandrose-like aggregates are formed. This potentially occurs due to the formation of micro-droplets, which can act as individual micro-reaction compartments. In contrast, thermolysis of homogeneously dissolved solutions of **1** in ILs of higher hydrophobicity, which increases with increasing alkyl

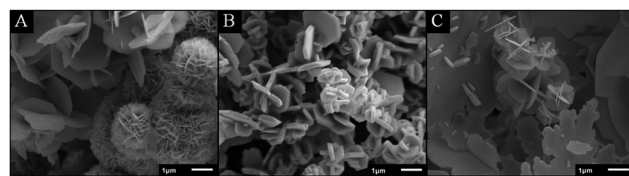


**Fig. 7** SEM images of  $\text{Sb}_2\text{Te}_3$  nanoparticles synthesized in  $\text{C}_4\text{C}_4\text{ImBr}$  (A),  $\text{C}_6\text{C}_6\text{ImBr}$  (B) and  $\text{C}_8\text{C}_8\text{ImBr}$  (C).

chain length, leads to a steady growth of the  $\text{Sb}_2\text{Te}_3$  nanoparticles. Finally the microstructure of the IL can help to guide the particle growth.  $\text{C}_8\text{C}_8\text{imBr}$  prefers the formation of a lamellar structure and thus favours the sheet-like growth of  $\text{Sb}_2\text{Te}_3$  nanoplates.

**Thermoelectric transport properties.** To investigate how the nanostructure of the obtained  $\text{Sb}_2\text{Te}_3$  material is correlated to the thermoelectric transport properties these samples were investigated in detail. For the characterization of thermoelectric transport properties, the  $\text{Sb}_2\text{Te}_3$  nanoparticles were cold pressed to macroscopic pellets and subsequently annealed at 300 °C. After the determination of the thermoelectric transport properties, we re-investigated the material composition by EDX and XRD. According to these results we can exclude any change of the material composition as well as the formation of any additional crystalline phase during the processing process. Fig. 8 exemplarily shows two powder X-ray diffractograms of a  $\text{Sb}_2\text{Te}_3$  sample before and after processing.

*Variation of the different alkyl-chain lengths of symmetric imidazolium-based ILs  $\text{C}_n\text{C}_n\text{imBr}$ .* Since the influence of the alkyl chain lengths was observed for both the unsymmetrically and symmetrically substituted imidazolium derivatives, detailed transport characterization was performed with the nanoparticles obtained from the symmetrically substituted ILs.

Fig. 8 shows the cross-section SEM images of the three pellets as-obtained from samples synthesized in  $\text{C}_4\text{C}_4\text{imBr}$  (C<sub>4</sub>) (Fig. 8A),  $\text{C}_6\text{C}_6\text{imBr}$  (C<sub>6</sub>) (Fig. 8B) and  $\text{C}_8\text{C}_8\text{imBr}$  (C<sub>8</sub>) (Fig. 8C), respectively. Distinct differences between the characteristic microstructure of the three samples after the cold pressing compaction can be seen, which can be directly correlated to the morphology of the  $\text{Sb}_2\text{Te}_3$  nanoparticles from the IL.

In  $\text{C}_4\text{C}_4\text{imBr}$  the formation of sandroses (Fig. 7A) prevailed and this microstructure is maintained in the cold pressed samples where individual spheres can be made out (Fig. 9A). In  $\text{C}_6\text{C}_6\text{imBr}$  random three dimensional aggregations of these particles occurred (Fig. 7B) and this also shows in the

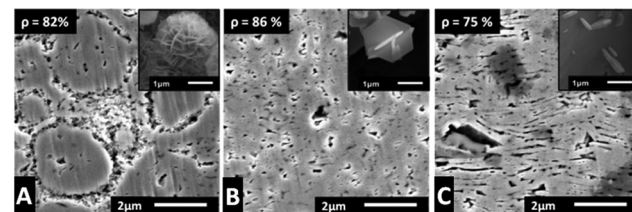


Fig. 9 Cross section SEM images of the three cold pressed  $\text{Sb}_2\text{Te}_3$  bulk samples synthesized in the ionic liquids  $\text{C}_4\text{C}_4\text{imBr}$  (C<sub>4</sub>) (A),  $\text{C}_6\text{C}_6\text{imBr}$  (C<sub>6</sub>) (B) and  $\text{C}_8\text{C}_8\text{imBr}$  (C<sub>8</sub>) (C); insets: SEM micrographs for the respective non-pressed samples.

compacted sample (Fig. 9B). In  $\text{C}_8\text{C}_8\text{imBr}$  the formation of large, extended nanosheets took place (Fig. 7C) and the SEM image of the cross section pellets shows still individual sheets that are stacked parallel (Fig. 9C). The microstructure evoked by the individual particle morphology and aggregation impacts directly the densities of the compacted samples. The density of the samples is  $5.3 \text{ g cm}^{-3}$  (82%) for  $\text{C}_4\text{C}_4\text{imBr}$ ,  $5.7 \text{ g cm}^{-3}$  (86%) for  $\text{C}_6\text{C}_6\text{imBr}$ , and  $4.9 \text{ g cm}^{-3}$  (75%) for  $\text{C}_8\text{C}_8\text{imBr}$ , respectively.

Fig. 10 shows the thermoelectric transport properties of the three samples between room temperature and 573 K. Table 1 summarizes the thermoelectric transport data of these three pellets at room temperature. The Seebeck coefficients range from  $140 \mu\text{V K}^{-1}$  to  $180 \mu\text{V K}^{-1}$ . The decomposition of **1** was shown to produce  $\text{Sb}_2\text{Te}_3$  nanoparticles with a highly stoichiometric composition and low anti-site defect concentration, resulting in high values of the Seebeck coefficient as observed in our previous study.<sup>12a</sup> This is observed here, too.

The Hall carrier concentrations  $n_{\text{H}}$  are  $5.5 \times 10^{19} \text{ cm}^{-3}$  ( $\text{C}_4\text{C}_4\text{imBr}$ ),  $4.9 \times 10^{19} \text{ cm}^{-3}$  ( $\text{C}_6\text{C}_6\text{imBr}$ ) and  $3.1 \times 10^{19} \text{ cm}^{-3}$  ( $\text{C}_8\text{C}_8\text{imBr}$ ). The samples show a high variation in the electrical conductivity  $\sigma$ . The highest  $\sigma$  of  $463 \text{ S cm}^{-1}$  at room temperature was observed for the sample synthesized in  $\text{C}_4\text{C}_4\text{imBr}$  and is smaller for the samples prepared in  $\text{C}_6\text{C}_6\text{imBr}$  ( $272 \text{ S cm}^{-1}$ ) and  $\text{C}_8\text{C}_8\text{imBr}$  ( $145 \text{ S cm}^{-1}$ ).

From the electrical conductivity and the Hall carrier concentration, we obtained the Hall mobility of the charge carriers,  $\mu_{\text{H}}$ , which was corrected for the electrically active volume of the material (Fig. 11).

For this, the value was normalized to the relative density of the samples.<sup>25</sup> With this correction for the density, the Hall mobilities  $\mu_{\text{H}}$  of  $64 \text{ cm}^2 \text{ V}^{-1} \text{ s}^{-1}$  ( $\text{C}_4\text{C}_4\text{imBr}$ ),  $41 \text{ cm}^2 \text{ V}^{-1} \text{ s}^{-1}$  ( $\text{C}_6\text{C}_6\text{imBr}$ ) and  $39 \text{ cm}^2 \text{ V}^{-1} \text{ s}^{-1}$  ( $\text{C}_8\text{C}_8\text{imBr}$ ) were found. There is no evident trend of the Hall mobility and the electrical conductivity with respect to the varying densities of the three samples, instead the mobility decreases with increasing chain length. Due to the nanostructure of the samples, the thermal conductivity could be reduced from  $5.6 \text{ W m}^{-1} \text{ K}^{-1}$  parallel  $\parallel$  and  $1.6 \text{ W m}^{-1} \text{ K}^{-1}$   $\perp$  perpendicular to the *c*-direction<sup>26</sup> for a single crystalline  $\text{Sb}_2\text{Te}_3$  in the range of  $0.49\text{--}0.72 \text{ W m}^{-1} \text{ K}^{-1}$ , comparable with values previously reported by Mehta *et al.* for  $\text{Sb}_2\text{Te}_3$  nanoparticles.<sup>27</sup> At 490 K the thermal conductivity exhibits a minimum in all samples and

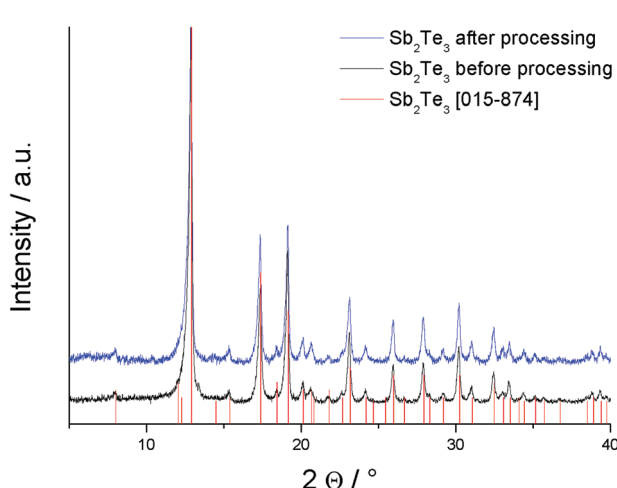


Fig. 8 PXRDs of a  $\text{Sb}_2\text{Te}_3$  sample before and after processing (with Mo  $\text{K}\alpha$  radiation).



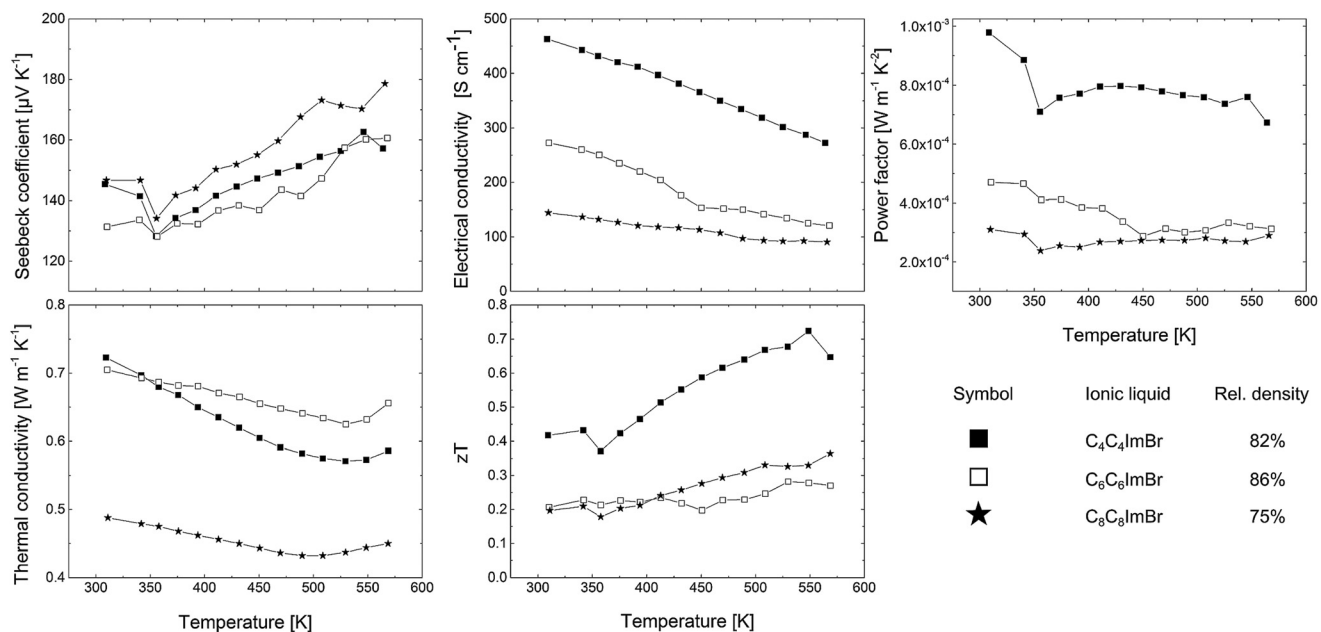


Fig. 10 Thermoelectric transport properties of three  $\text{Sb}_2\text{Te}_3$  bulk samples synthesized in  $\text{C}_4\text{C}_4\text{ImBr}$ ,  $\text{C}_6\text{C}_6\text{ImBr}$  and  $\text{C}_8\text{C}_8\text{ImBr}$ .

**Table 1** Density, rel. density, Hall carrier concentration  $n_{\text{H}}$ , Hall mobility  $\mu_{\text{H}}$  overall and in the electrically active volume, electrical conductivity  $\sigma$ , thermal conductivity  $\kappa$ , lattice thermal conductivity  $\kappa_{\text{L}}$ , and Seebeck coefficient  $\alpha$  at 300 K

| Sample                                                                 | $\text{C}_4$                      | $\text{C}_6$                      | $\text{C}_8$                      |
|------------------------------------------------------------------------|-----------------------------------|-----------------------------------|-----------------------------------|
| Ionic liquid                                                           | $\text{C}_4\text{C}_4\text{ImBr}$ | $\text{C}_6\text{C}_6\text{ImBr}$ | $\text{C}_8\text{C}_8\text{ImBr}$ |
| Density [g cm <sup>-3</sup> ]                                          | 5.3                               | 5.7                               | 4.9                               |
| Relative density [%]                                                   | 82                                | 86                                | 75                                |
| $n_{\text{H}} [\times 10^{19} \text{ cm}^{-3}]$ – overall              | 5.5                               | 4.9                               | 3.1                               |
| $\mu_{\text{H}} [\text{cm}^2 \text{ V}^{-1} \text{ s}^{-1}]$ – overall | 53                                | 35                                | 29                                |
| – In electrically active volume                                        | 64                                | 41                                | 39                                |
| $\sigma [\text{S cm}^{-1}]$                                            | 463                               | 272                               | 145                               |
| $\kappa [\text{W m}^{-1} \text{ K}^{-1}]$                              | 0.72                              | 0.71                              | 0.49                              |
| $\kappa_{\text{L}} [\text{W m}^{-1} \text{ K}^{-1}]$                   | 0.44                              | 0.59                              | 0.39                              |
| $\alpha [\mu\text{V K}^{-1}]$                                          | 145                               | 131                               | 147                               |

increases at higher temperatures. To calculate the lattice thermal conductivity, we subtracted the electronic contribution  $\kappa_{\text{e}}$  from the total thermal conductivity, estimated from the Wiedemann-Franz dependence,  $\kappa_{\text{e}} = \sigma LT$ . For this, the literature value of the Lorenz number ( $L = 1.72 \times 10^{-8} \text{ W } \Omega \text{ K}^{-2}$  Single Parabolic Band Model)<sup>28</sup> was used considering a temperature independent  $L$ .

Fig. 12 clearly shows that the lattice thermal conductivity still increases. This is most likely caused by the bipolar effect known to appear in this temperature range for semiconductors with a small band gap ( $\text{Sb}_2\text{Te}_3$ : band gap  $E_g = 0.28 \text{ eV}^{29}$ ): at a certain temperature electron-hole-pairs are generated and an additional contribution for the thermal conductivity  $\kappa$  from the bipolar thermal conductivity  $\kappa_{\text{b}}$  is given. While the thermal conductivity data points towards a contribution of the bipolar effect, in principle this effect should also influence the other transport coefficients, *i.e.* decrease the Seebeck coefficient and

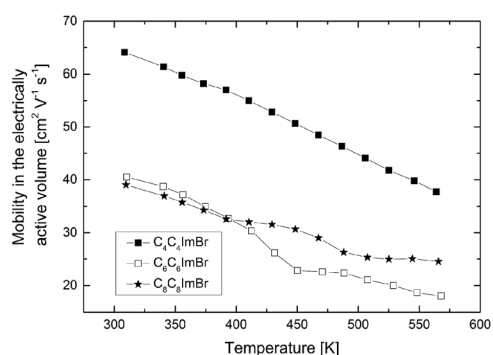


Fig. 11 Mobility in the electrically active volume plotted as a function of temperature for samples obtained from the respective ionic liquids.

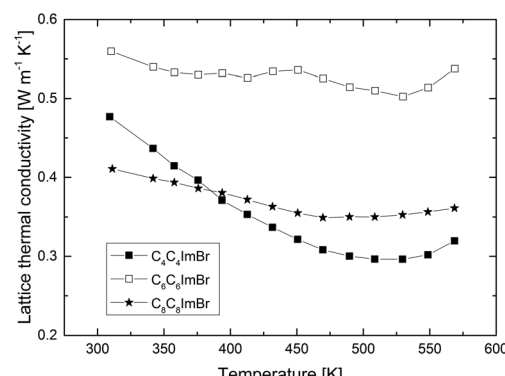


Fig. 12 Lattice thermal conductivity in dependence of the temperature.

increase the electrical conductivity due to minority carriers, which is not seen here.

The most promising property combination of the transport properties is found for samples synthesized in  $C_4C_4imBr$ , which exhibited the highest charge carrier concentration, the highest charge carrier mobility and the lowest lattice thermal conductivity. The figure of merit  $zT$  reaches a maximum value of 0.72 at 550 K for the  $C_4C_4imBr$  sample (Fig. 10).

From this we conclude that the formation of individual sandrose nanostructures of  $Sb_2Te_3$  that can be maintained in the compacted samples, gives the best combination of properties leading to high  $zT$  values. Thus, short chain length IL cations are beneficial for this. To check this hypothesis, the thermoelectric transport properties of samples obtained from ILs with short chain imidazolium cations ( $C_4mim$ ) in combination with various anions that gave sandrose-like nanostructures are investigated.

*Role of the anion of 1-butyl-3-methyl-imidazolium based ILs in thermoelectric properties.* In order to investigate the role of the anion in the thermoelectric properties of the resulting  $Sb_2Te_3$  nanoparticles in more detail, four  $Sb_2Te_3$  samples were

prepared under analogous reaction conditions in  $C_4mimCl$  (A),  $C_4mimBr$  (B),  $C_4mimI$  (C) and  $C_4mimNTf_2$  (D), respectively, and then compacted to  $Sb_2Te_3$  pellets using the same protocol. Cross section pictures (Fig. 13) of the resulting cold pressed pellets clearly demonstrate that the agglomerate structure as observed in the SEM pictures of the nanoparticles is preserved within the microstructure of the pellets (Fig. 13A–D).  $Sb_2Te_3$  synthesized in  $C_4mimNTf_2$  shows only a few agglomerates in the microstructure (Fig. 13D), whilst for those observed from  $C_4mimCl$  shows that those rose-like structures are still preserved.

Table 2 summarizes the thermoelectric transport properties for the four samples synthesized in  $C_4mimCl$ ,  $C_4mimBr$ ,  $C_4mimI$  and  $C_4mimNTf_2$  at 300 K. The density of the compressed pellets are  $5.1 \text{ g cm}^{-3}$  (79%,  $C_4mimCl$ ),  $5.2 \text{ g cm}^{-3}$  (80%,  $C_4mimBr$ ),  $5.5 \text{ g cm}^{-3}$  (85%,  $C_4mimI$ ) and  $5.3 \text{ g cm}^{-3}$  (82%,  $C_4mimNTf_2$ ), respectively.

In Fig. 14 the thermoelectric transport properties are presented. The Seebeck coefficient for all samples ranges from 130 to  $170 \mu\text{V K}^{-1}$  in the temperature range between room temperature and 573 K, which is comparable to the values of the samples discussed before. The highest electrical conductivity of  $870 \text{ S cm}^{-1}$  at room temperature was found for the sample synthesized in  $C_4mimI$ , whereas that prepared in  $C_4mimNTf_2$  ( $397 \text{ S cm}^{-1}$ ),  $C_4mimCl$  ( $293 \text{ S cm}^{-1}$ ) and  $C_4mimBr$  ( $264 \text{ S cm}^{-1}$ ) showed significantly lower values. The thermal conductivity is  $1.1 \text{ W m}^{-1} \text{ K}^{-1}$  for the sample obtained from  $C_4mimNTf_2$ ,  $0.89 \text{ W m}^{-1} \text{ K}^{-1}$  for that from  $C_4mimI$ ,  $0.72 \text{ W m}^{-1} \text{ K}^{-1}$  for that from  $C_4mimBr$  and  $0.56 \text{ W m}^{-1} \text{ K}^{-1}$  for that from  $C_4mimCl$ . The electrical and thermal conductivities show a dependence on the density of the samples. The highest values for  $\sigma$  and  $\kappa$  are measured for the samples with densities of 85% ( $C_4mimI$ ) and 82% ( $C_4mimNTf_2$ ) and are smaller for the  $Sb_2Te_3$  pellets with 80% ( $C_4mimBr$ ) and 79% ( $C_4mimCl$ ). The highest  $zT$  value of 0.93 at 260 °C is reached for  $C_4mimI$ , and for the other samples the  $zT$  values are between 0.35 ( $C_4mimBr$ ) and 0.44 ( $C_4mimNTf_2$ ,  $C_4mimCl$ ).

By correlating the thermal transport data with the particle morphologies it is evident that the concept of controlling the thermal conductivity through phonon phase boundary scattering by a nanotemplating effect of the IL has been successful: in the case where small, individual nano-sandroses could be obtained by using an ionic liquid of high polarity with a

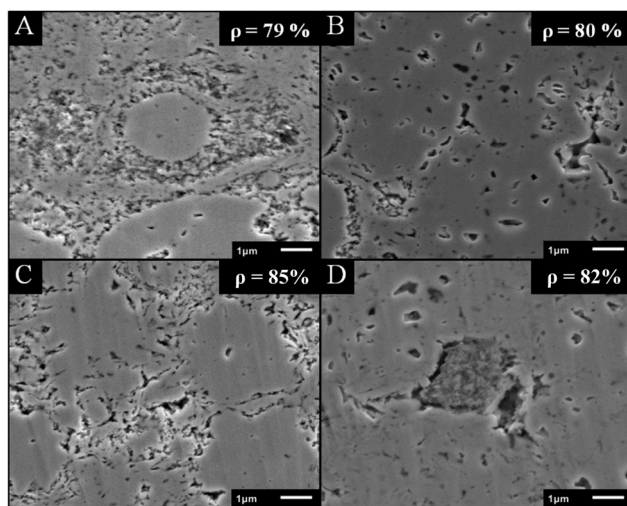


Fig. 13 Cross section SEM images of four cold pressed  $Sb_2Te_3$  bulk samples synthesized in  $C_4mimCl$  (A),  $C_4mimBr$  (B),  $C_4mimI$  (C) and  $C_4mimNTf_2$  (D).

Table 2 Density, rel. density, Hall carrier concentration  $n_H$  and the Hall mobility  $\mu_H$  overall and in the electrically active volume, electrical conductivity  $\sigma$ , thermal conductivity  $\kappa$ , lattice thermal conductivity  $\kappa_L$ , and Seebeck coefficient  $\alpha$  at 300 K

| Sample                                                            | Cl         | Br         | I         | NTf <sup>2</sup> |
|-------------------------------------------------------------------|------------|------------|-----------|------------------|
| Ionic liquid                                                      | $C_4mimCl$ | $C_4mimBr$ | $C_4mimI$ | $C_4mimNTf_2$    |
| Density [g cm <sup>-3</sup> ]                                     | 5.1        | 5.2        | 5.5       | 5.3              |
| Relative density [%]                                              | 79         | 80         | 85        | 82               |
| $n_H$ [ $\times 10^{19} \text{ cm}^{-3}$ ] – overall              | 9.7        | 3.8        | 5.7       | 7.1              |
| $\mu_H$ [ $\text{cm}^2 \text{ V}^{-1} \text{ s}^{-1}$ ] – overall | 19         | 43         | 95        | 35               |
| – In electrically active volume                                   | 24         | 54         | 112       | 42               |
| $\sigma$ [ $\text{S cm}^{-1}$ ]                                   | 291        | 264        | 869       | 393              |
| $\kappa$ [ $\text{W m}^{-1} \text{ K}^{-1}$ ]                     | 0.56       | 0.72       | 0.89      | 1.1              |
| $\alpha$ [ $\mu\text{V K}^{-1}$ ]                                 | 150        | 133        | 135       | 150              |

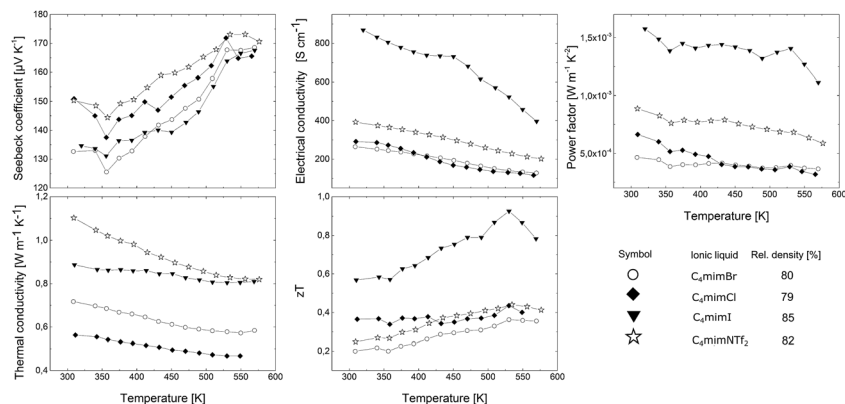


Fig. 14 Thermoelectric transport properties of four  $\text{Sb}_2\text{Te}_3$  bulk samples synthesized in  $\text{C}_4\text{mimBr}$ ,  $\text{C}_4\text{mimCl}$ ,  $\text{C}_4\text{mimI}$ , and  $\text{C}_4\text{mimNTf}_2$ .

strongly coordinating anion, the compacted material exhibited the lowest thermal conductivity.

The electrical Hall mobility shows a clear trend for the samples synthesized in the ionic liquids  $\text{C}_4\text{mimCl}$ ,  $\text{C}_4\text{mimBr}$ , and  $\text{C}_4\text{mimI}$ , with increasing  $\mu_H$  from  $24 \text{ cm}^2 \text{ V}^{-1} \text{ s}^{-1}$  to  $112 \text{ cm}^2 \text{ V}^{-1} \text{ s}^{-1}$ . This correlates with the trend found in the morphology of the respective nanoparticles which show an increasing thickness of the nanoparticle platelets with increasing atomic number of the halide anion (compare Fig. 4). It is assumed that the nanoparticle platelets orient – at least partly – during the compaction process perpendicular to the pressing direction. All transport properties are characterized in the pressing direction of the pellets. Therefore, with increasing thickness of the platelets, there are less scattering events for both, electrons and phonons, and consequently the highest values for the electrical Hall mobility and also the thermal conductivity are reached. However, looking at the ionic radii of the IL anions used for the synthesis, it becomes

clear that the ionic radius of an  $\text{I}^-$  ion (220 pm) is very similar to that of a  $\text{Te}^{2-}$  ion (221 pm).<sup>30</sup> Thus, it appears possible that small amounts of  $\text{I}^-$  can replace  $\text{Te}^{2-}$  in the structure of  $\text{Sb}_2\text{Te}_3$ , which could also influence the electronic transport properties. More theoretical and experimental evidence will be needed to further substantiate this hypothesis.

*Comparison of zT values.* Within the following paragraph we compare our results with the literature state of the art. Table 3 shows the  $zT$  of nanostructured  $\text{Sb}_2\text{Te}_3$  samples for different synthesis routes.

Within this comparison, Snyder and Toberer<sup>31</sup> report the  $zT$  data by Marlow Industries that reach  $zT \geq 0.8$  at 400 K for  $\text{Sb}_2\text{Te}_3$ -based alloys (not further specified). By co-doping  $\text{Sb}_2\text{Te}_3$  with sulphur, Mehta *et al.* demonstrate  $zT \geq 0.92$  at 400 K.<sup>27</sup> Phase pure  $\text{Sb}_2\text{Te}_3$ , without any alloying or co-coping, was investigated by Heimann *et al.* within an earlier work of this group.<sup>12a</sup> Hereby, the microwave-assisted decomposition of the SSP  $(\text{Et}_2\text{Sb})_2\text{Te}$  in ionic liquids enhanced the  $zT$  value

Table 3 Compilation of the  $\text{Sb}_2\text{Te}_3$  figure of merit data at 400 K, comparing the data with literature references

| Synthesis method                                                                                                        | $zT$ (300 K) | $zT$ (400 K) | Ref.                                |
|-------------------------------------------------------------------------------------------------------------------------|--------------|--------------|-------------------------------------|
| Thermal decomposition of SSP in the IL $\text{C}_4\text{mimI}$                                                          | 0.59         | 0.65         | <sup>a</sup>                        |
| Commercial alloys, mostly based on $\text{Sb}_2\text{Te}_3$                                                             | 1            | 0.8          | Snyder (2008) <sup>31</sup>         |
| Solvothermal (MW-assisted); $\text{SbCl}_3 + \text{Na}_2\text{TeO}_3 + \text{N}_2\text{H}_4$ hydrate in EG <sup>b</sup> | 0.15         | 0.46         | Dong (2010) <sup>32</sup>           |
| S-doped $\text{Sb}_2\text{Te}_3$ NPs                                                                                    | 0.7          | 0.92         | Mehta (2012) <sup>27</sup>          |
| Solvothermal, template-free                                                                                             | 0.22*        | 0.35         | Sun (2013) <sup>33</sup>            |
| Co-precipitation followed by wet Chemical reduction                                                                     | 0.03*        | 0.12         | Saleemi (2014) <sup>34</sup>        |
| Thermal decomposition of SSP <sup>c</sup> in IL                                                                         |              |              | Heimann (2015) <sup>12a</sup>       |
| (a) Thermal (oil bath)                                                                                                  | 0.4          | 0.5          |                                     |
| (b) MW-assisted                                                                                                         | 0.75         | 1.1          |                                     |
| Solvothermal; $\text{SbCl}_3 + \text{Te}$ powder + alkaline 2,7-DHN in the presence of CTAB                             | 0.001        |              | Nithiyanantham (2015) <sup>35</sup> |
| Physical vapor deposition (PVD); $\text{Sb}_2\text{Te}_{3-x}\text{S}_x$ platelets                                       |              |              | Thankamma (2015) <sup>36</sup>      |
| -Without doping $x = 0$                                                                                                 | 0.22         |              |                                     |
| -With the S-content $x = 0.3$                                                                                           | 0.54         |              |                                     |
| Solvothermal; $\text{Sb}_2\text{Te}_3$ wires; $\text{Sb} + \text{Te}$ in EG                                             | 0.32*        | 0.44         | Yang (2016) <sup>37</sup>           |

<sup>a</sup>This paper. <sup>b</sup>EG = ethylene glycol. <sup>c</sup>SSP = single source precursor. The marked values (\*) were interpolated from the literature data for 300 K for comparison.

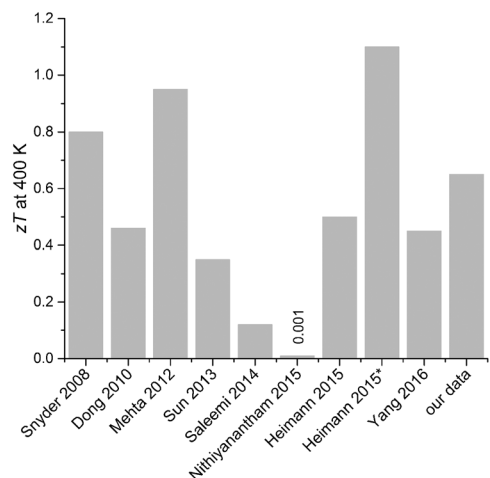


**Fig. 15** Compilation of the  $\text{Sb}_2\text{Te}_3$  figure of merit data at 400 K, comparing the data with literature references. Heimann 2015 describes the thermal decomposition in an oil bath and Heimann 2015\* in a laboratory microwave oven.

from  $zT \approx 0.5$  to  $zT \approx 1.1$  at 400 K. Within this work we systematically studied the influence of different ILs and report  $zT$  values that match this range of literature values, see graphical compilation in Fig. 15.

## Conclusions

The morphology of  $\text{Sb}_2\text{Te}_3$  nanoparticles synthesized in 1-alkyl-3-methylimidazolium- and 1,3-dialkylimidazolium-based ILs strongly depends on the chain length of the alkyl group of the IL cation (Fig. 16) and the Lewis basicity of the IL anion (Fig. 17).

An increasing chain length resulted in better solubility of the single source precursor  $(\text{Et}_2\text{Sb})_2\text{Te}$ , which enhanced the formation of less aggregated nanoparticles. In addition, the role of the anion is mainly attributed to its basicity and its capability to bind to the growing nanoparticle surface. Stronger bases were found to more effectively block the

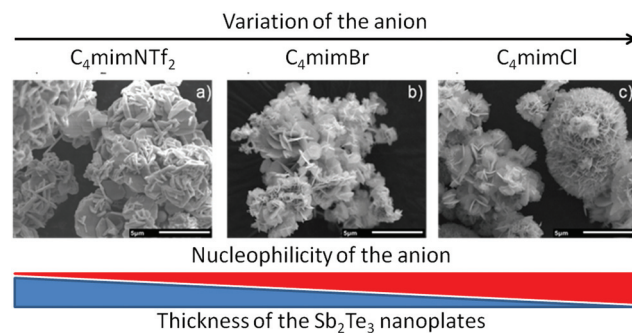


**Fig. 17** Morphology-directing effect of the IL anion.

surface, resulting in the formation of thin  $\text{Sb}_2\text{Te}_3$  nanoplates, while the formation of thicker nanoparticles was observed with decreasing basicity. As a consequence, the thermoelectric properties of the resulting  $\text{Sb}_2\text{Te}_3$  nanoplates strongly differed. Identification of the distinctive roles of the IL anion and cation may help to further improve the figure of merit for these types of materials in the near future.

## Experimental

### Synthetic procedures

Synthetic procedures and thermolysis experiments were performed under inert conditions (Ar atmosphere) in a glovebox or using standard Schlenk techniques. Solvents were dried over Na/K alloy and degassed prior to use. **1** was prepared according to a literature method.<sup>38</sup> 1-N-Methylimidazolium (99%, Sigma Aldrich), 1-halobutanes (99%, Acros) and  $\text{CH}_3\text{CN}$  (99.9%+, Extra Dry, Acros) were commercially available. 1-Alkyl-3-methylimidazolium ( $\text{C}_n\text{mim}$ ;  $n = 3\text{--}8$ ) and 1,3-dialkylimidazolium-based ILs ( $\text{C}_n\text{C}_x\text{mim}$ ;  $n = 4, 6$  and 8) were prepared by literature methods.<sup>12,39</sup>

### Materials and methods

**Microwave synthesis of  $\text{Sb}_2\text{Te}_3$  nanoparticles.** 1.18 g (2.42 mmol) of **1** was added to 13.7 mmol of the respective ionic liquid. The room temperature solid ILs  $\text{C}_4\text{mimCl}$ ,  $\text{C}_x\text{mimBr}$  ( $x = 3\text{--}5$ ) and  $\text{C}_x\text{C}_x\text{mimBr}$  ( $x = 4, 6, 8$ ) were molten by heating to 90 °C before adding **1**. The reaction mixture was stirred for 5 min and heated in a laboratory microwave oven (Discover, CEM) for 30 s at 100 °C, subsequently for 5 s at 150 °C and finally for 5 min at 170 °C. The heating was performed with a maximum power of 100 W until the desired temperature was reached and kept at that temperature with a power of 5–12 W. The reaction container was cooled with compressed air with a pressure of 100 kPa. The resulting colloidal solutions were centrifuged (2000 rpm), washed with 10 mL of acetonitrile (7×) and dried at ambient temperature under dynamic vacuum.

### Material characterization

**Electron microscopy.** The particle size and morphology as well as the elemental composition of the nanoparticles and of

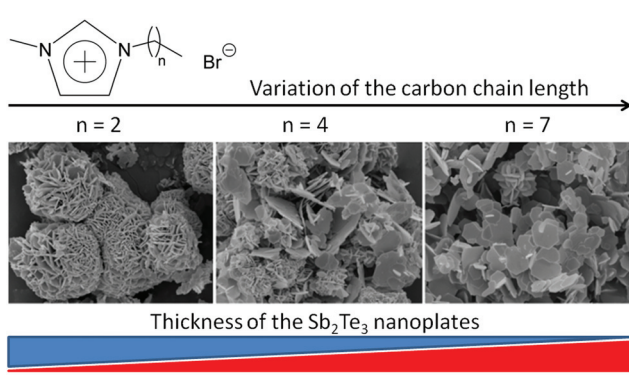


**Fig. 16** Morphology-directing effect of the IL cation.

cross section samples of the  $\text{Sb}_2\text{Te}_3$  pellets, which were prepared using a Jeol Cross Section Polisher (IB-09010CP), were analysed by scanning electron microscopy (SEM) using a Jeol JSM 6510 microscope equipped with a Bruker Quantax 400 unit (EDX).

**Powder X-ray analysis.** PXRD patterns were collected on powder filled Lindeman capillaries on a Huber 670 powder diffractometer with Mo K $\alpha$  radiation ( $\lambda$ : 0.71073 nm, 40 kV and 40 mA) or a Bruker D8 Advance powder diffractometer with Cu K $\alpha$  radiation ( $\lambda$ : 1.5418 Å, 40 kV and 40 mA) using a Si single crystal as a sample holder to minimize scattering. For better homogenization, the dried powder samples were re-dispersed in ethanol on the Si surface and investigated in the range from 10 to 90°  $2\theta$  with a step size of 0.01°  $2\theta$  (counting time 0.6 s). Rietveld refinements were performed with the program package TOPAS 4.2 (Bruker) to determine the lattice parameters and average crystallite size by using the Scherrer equation.<sup>26</sup> The structure model of  $\text{Sb}_2\text{Te}_3$  (#192780) from the ICSD database was used. For each Rietveld refinement, the instrumental correction as determined with a standard powder sample  $\text{LaB}_6$  from the NIST (National Institute of Standards and Technology) as the standard reference material (SRM 660b;  $a(\text{LaB}_6)$  = 4.15689 Å) was taken into account.

**Photoelectron spectroscopy.** The XPS measurements were done at a VersaProbe II by Ulvac-Phi. Monochromatic Al-K $\alpha$  light with  $h\nu$  = 1486.6 eV was used and the electron emission angle was 45°. All spectra were referenced to the position of the main carbon peak at 284.8 eV binding energy. The Sb 3d signal was fitted by first fitting the 3d<sub>3/2</sub> peaks and constraining the position and intensity of the 3d<sub>5/2</sub> components to these values. This is done in order to estimate the O 1s signal which overlaps with the Sb 3d<sub>5/2</sub> peaks. The samples were transported under an inert gas atmosphere to the XPS machine and were exposed to air for roughly 3 minutes prior to their insertion into a vacuum.

**Thermoelectric properties.** The nanocrystalline  $\text{Sb}_2\text{Te}_3$  powder was compressed to a pellet with a diameter of 5 mm applying a pressure of 815 MPa for 30 min. A pressing tool from Atlas Power 25T from SPECAC made from stainless steel was used. The density of the pellets was determined from the mass to volume ratio. Annealing was performed at 573 K in vacuum ( $10^{-5}$  mbar) with a ramp of 5 K min<sup>-1</sup> and a dwell time of one hour. All thermoelectric coefficients were measured in the z-direction corresponding to the pressing direction of the pellet in a temperature range from room temperature to 573 K. The Seebeck coefficient  $\alpha$  and the electrical conductivity  $\sigma$  were measured by using a commercial device ZEM-3 provided by Ulvac Technologies, Inc. The thermal conductivity  $\kappa$  is calculated with  $\kappa = D_T \rho c_p$  with  $D_T$  the thermal diffusivity,  $\rho$  the density and  $c_p$  the heat capacity. The thermal diffusivity was measured with an LFA 457 Microflash from NETZSCH-Gerätebau GmbH. For the calculation a literature value for the heat capacity was used.<sup>40</sup> Hall measurements were done at room temperature in the van-der-Pauw geometry with a Physical Property Measurement System (PPMS, Dyna Cool Series) provided by Quantum Design, Inc. From the measured Hall coefficient  $R_H$ , the Hall carrier concentration

$n_H$  is estimated, which is assumed to be isotropic and temperature independent. The Hall mobility was derived from the dependence  $\sigma = e\mu_H n_H$ .

## Acknowledgements

S. Schulz and G. Schierning gratefully acknowledge financial support by the Deutsche Forschungsgemeinschaft DFG within the priority program SPP 1708. The authors like to thank M. Sc. Georg Bendt (Faculty of Chemistry, University of Duisburg-Essen) for Rietveld refinements of selected samples.

## Notes and references

- 1 M. H. Elsheikh, D. A. Shnawah, M. F. M. Sabri, S. B. M. Said, M. H. Hassan, M. B. A. Bashir and M. Mohamad, *Renewable Sustainable Energy Rev.*, 2014, **30**, 337.
- 2 L. E. Bell, *Science*, 2008, **321**, 1457.
- 3 (a) D. M. Rowe, *CRC Handbook of Thermoelectrics*, CRC Press, Boca Raton, FL, 1995; (b) J. R. Drabble and C. H. L. Goodman, *J. Phys. Chem. Solids*, 1958, **5**, 142.
- 4 (a) R. Venkatasubramanian, E. Siivola, T. Colpitts and B. O'Quinn, *Nature*, 2001, **413**, 597; (b) T. C. Harman, P. J. Taylor, M. P. Walsh and B. E. LaForge, *Science*, 2002, **297**, 2229; (c) D. Hsieh, Y. Xia, D. Qian, L. Wray, F. Meier, J. H. Dil, J. Osterwalder, L. Patthey, A. V. Fedorov, H. Lin, A. Bansil, D. Grauer, Y. S. Hor, R. J. Cava and M. Z. Hasan, *Phys. Rev. Lett.*, 2009, **103**, 146401.
- 5 (a) H. Zhang, C.-X. Liu, X.-L. Qi, X. Dai, Z. Fang and S.-C. Zhang, *Nat. Phys.*, 2009, **5**, 438; (b) L. He, X. Kou and K. L. Wang, *Phys. Status Solidi RRL*, 2013, **7**, 50; (c) J. J. Cha, K. J. Koski and Y. Cui, *Phys. Status Solidi RRL*, 2013, **7**, 15; (d) G. Wang, X. Zhu, J. Wen, X. Chen, K. He, L. Wang, X. Ma, Y. Liu, X. Dai, Z. Fang, J. Jia and Q. Xue, *Nano Res.*, 2010, **3**, 874; (e) C. Pauly, G. Bihlmayer, M. Liebmann, M. Grob, A. Georgi, D. Subramaniam, M. R. Scholz, J. Sánchez-Barriga, A. Varykhalov, S. Blügel, O. Rader and M. Morgenstern, *Phys. Rev. B: Condens. Matter*, 2012, **86**, 235106.
- 6 (a) J. P. Heremans, M. S. Dresselhaus, L. E. Bell and D. T. Morelli, *Nat. Nanotechnol.*, 2013, **8**, 471; (b) J. Yang, H.-L. Yip and A. K.-Y. Jen, *Adv. Energy Mater.*, 2013, **3**, 549.
- 7 (a) N. Mingo, D. Hauser, N. P. Kobayashi, M. Plissonnier and A. Shakouri, *Nano Lett.*, 2009, **9**, 711; (b) B. Poudel, Q. Hao, Y. Ma, Y. Lan, A. Minnich, B. Yu, X. Yan, D. Wang, A. Muto, D. Vashaee, X. Chen, J. Liu, M. S. Dresselhaus, G. Chen and Z. Ren, *Science*, 2008, **320**, 634; (c) Z. Wang, J. E. Alaniz, W. Jang, J. E. Garay and C. Dames, *Nano Lett.*, 2011, **11**, 2206.
- 8 K. Biswas, J. He, I. D. Blum, C.-I. Wu, T. P. Hogan, D. N. Seidman, V. P. Dravid and M. G. Kanatzidis, *Nature*, 2012, **489**, 414.
- 9 (a) S. Schulz, S. Heimann, J. Friedrich, M. Engenhorst, G. Schierning and W. Assenmacher, *Chem. Mater.*, 2012,





24, 2228; (b) G. Bendt, A. Weber, S. Heimann, W. Assenmacher, O. Prymak and S. Schulz, *Dalton Trans.*, 2015, **44**, 14272.

10 S. Zastrow, J. Gooth, T. Boehnert, S. Heiderich, W. Toellner, S. Heimann, S. Schulz and K. Nielsch, *Semicond. Sci. Technol.*, 2013, **28**, 035010.

11 (a) G. Bendt, S. Schulz, S. Zastrow and K. Nielsch, *Chem. Vap. Deposition*, 2013, **19**, 235; (b) G. Bendt, S. Zastrow, K. Nielsch, P. S. Mandal, J. Sánchez-Barriga, O. Rader and S. Schulz, *J. Mater. Chem. A*, 2014, **2**, 8215; (c) S. Schulz, G. Bendt, J. Sonntag, A. Lorke, U. Hagemann and W. Assenmacher, *Semicond. Sci. Technol.*, 2015, **30**, 085021.

12 (a) S. Heimann, S. Schulz, J. Schaumann, A. Mudring, J. Stötzl and G. Schierning, *J. Mater. Chem. C*, 2015, **3**, 10375; (b) M. Loor, G. Bendt, U. Hagemann, C. Wölper, W. Assenmacher and S. Schulz, *Dalton Trans.*, 2016, **45**, 15326; (c) M. Loor, G. Bendt, J. Schaumann, U. Hagemann, M. Heidelmann, C. Wölper and S. Schulz, *Z. Anorg. Allg. Chem.*, DOI: 10.1002/zaac.201600325.

13 (a) C. Lorbeer, J. Cybinska and A.-V. Mudring, *Cryst. Growth Des.*, 2011, **11**, 1040; (b) T. Alammar and A.-V. Mudring, *ChemSusChem*, 2011, **12**, 1796; (c) T. Alammar, O. Shekhah, J. Wohlgemuth and A.-V. Mudring, *J. Mater. Chem.*, 2012, **22**, 18252.

14 (a) T. Alammar, H. Noei, Y. Wang and A.-V. Mudring, *Nanoscale*, 2013, **5**, 8045; (b) C. Lorbeer and A.-V. Mudring, *Chem. Commun.*, 2014, **50**, 13282.

15 (a) L. Crowhurst, P. R. Mawdsley, J. M. Perez-Arlandis, P. A. Salter and T. Welton, *Phys. Chem. Chem. Phys.*, 2003, **5**, 2790S; (b) S. Pitula and A.-V. Mudring, *Phys. Chem. Chem. Phys.*, 2010, **12**, 7056; (c) J. Bartosik and A.-V. Mudring, *Phys. Chem. Chem. Phys.*, 2010, **12**, 4005; (d) A. Babai, G. Kopiec, A. Lackmann, B. Mallick, S. Pitula, S.-F. Tang and A.-V. Mudring, *J. Mol. Liq.*, 2014, **92**, 191.

16 P. Wasserscheid and W. Keim, *Angew. Chem., Int. Ed.*, 2000, **39**, 3772.

17 (a) T. Alammar, K. Chow and A.-V. Mudring, *New J. Chem.*, 2015, **39**, 1339; (b) T. Alammar, H. Noei, Y. Wang, W. Grünert and A.-V. Mudring, *ACS Sustainable Chem. Eng.*, 2015, **3**, 42; (c) T. Alammar, I. Hamm, M. Wark and A.-V. Mudring, *Appl. Catal., B*, 2015, **178**, 20.

18 P. Ghosh, S.-F. Tang and A.-V. Mudring, *J. Mater. Chem.*, 2011, **21**, 8640.

19 (a) A. Mele, C. D. Tran and S. H. De Paoli Lacerda, *Angew. Chem., Int. Ed.*, 2003, **42**, 4364; (b) F. Castiglione, R. Simonutti, M. Mauri and A. Mele, *J. Phys. Chem. Lett.*, 2013, **4**, 1608; (c) J. C. Araque, J. J. Hettige and C. J. Margulis, *J. Phys. Chem. B*, 2015, **119**, 12727; (d) O. Russina, W. Schroer and A. Triolo, *J. Mol. Liq.*, 2015, **210**, 161; (e) W. D. Amith, J. J. Hettige, E. W. Castner and C. J. Margulis, *J. Phys. Chem. Lett.*, 2016, **7**, 3785.

20 (a) J. Canongia Lopes, M. F. Costa Gomes and A. A. H. Pádua, *J. Phys. Chem. B*, 2006, **110**, 16816; (b) M. Yang, P. Campbell, C. Santini and A.-V. Mudring, *Nanoscale*, 2014, **6**, 3367; (c) R. Hayes and G. G. Warr, *Chem. Rev.*, 2015, **115**, 6357.

21 (a) M. Yang, B. Mallick and A.-V. Mudring, *Cryst. Growth Des.*, 2013, **13**, 3068; (b) M. Yang, B. Mallick and A.-V. Mudring, *Cryst. Growth Des.*, 2014, **14**, 1561; (c) A. Getsis and A.-V. Mudring, *Cryst. Res. Technol.*, 2008, **43**, 1187; (d) M. Yang, K. Stappert and A.-V. Mudring, *J. Mater. Chem. C*, 2014, **2**, 458; (e) M. Yang, B. Mallick and A.-V. Mudring, *Cryst. Growth Des.*, 2013, **13**, 3068.

22 A. Taubert, *Angew. Chem., Int. Ed.*, 2004, **43**, 5380.

23 Sb values: (a) G. Chen, J. Zhou, J. Zuo and Q. Yang, *Appl. Mater. Interfaces*, 2016, **8**, 2819; (b) C. D. Wagner, A. V. Naumkin, A. Kraut-Vass, J. W. Allison, C. J. Powell and J. R. Rumble Jr., *NIST Standard Reference Database 20, Version 3.4 (web version)*, (<http://srdata.nist.gov/xps/>), 2003; (c) G. Gupta and J. Kim, *Dalton Trans.*, 2013, **42**, 8209; (d) M.-J. Shin, D.-J. Choi, M.-J. Kang, S.-Y. Choi, I.-W. Jang, K.-N. Lee and Y.-J. Park, *J. Korean Phys. Soc.*, 2004, **44**, 10. Te values: (e) C. D. Wagner, A. V. Naumkin, A. Kraut-Vass, J. W. Allison, C. J. Powell and J. R. Rumble Jr., *NIST Standard Reference Database 20, Version 3.4 (web version)*, (<http://srdata.nist.gov/xps/>), 2003; (f) H. Bando, K. Koizumi, Y. Oikawa, K. Daikohara, V. A. Kulbachinskii and H. Ozaki, *J. Phys.: Condens. Matter*, 2000, **12**, 5607; (g) C. R. Thomas, M. K. Vallon, M. G. Frith, H. Sezen, S. K. Kushwaha, R. J. Cava, J. Schwartz and S. L. Bernasek, *Chem. Mater.*, 2016, **28**, 35; (h) E. J. Menke, M. A. Brown, Q. Li, J. C. Hemminger and R. M. Penner, *Langmuir*, 2006, **22**, 10564.

24 B. Lv, S. Hu, W. Li, X. Di, L. Feng, J. Zhang, L. Wu, Y. Cai, B. Li and Z. Lei, *Int. J. Photoenergy*, 2010, 476589.

25 D. Gautam, M. Engenhorst, C. Schilling, G. Schierning, R. Schmechel and M. Winterer, *J. Mater. Chem. A*, 2015, **3**, 189.

26 H. Scherrer and S. Scherrer, in *CRC Thermoelectrics Handbook*, ed. D. M. Rowe, CRC Press, 2006, vol. 1, p. 407.

27 R. J. Mehta, Y. Zhang, C. Karthik, B. Singh, R. W. Siegel, T. Borca-Tasciuc and G. Ramanath, *Nat. Mater.*, 2012, **11**, 223.

28 A. F. May and G. J. Snyder, in *Materials, preparation, and characterization in thermoelectric*, 1, ed. D. M. Rowe, CRC Press, 2012, p. 11.

29 R. Sehr and L. R. Testardi, *J. Phys. Chem. Solids*, 1962, **23**, 1219.

30 R. D. Shannon, *Acta Crystallogr., Sect. A: Cryst. Phys., Diffr., Theor. Gen. Cryst.*, 1976, **32**, 751.

31 G. J. Snyder and E. S. Toberer, *Nat. Mater.*, 2008, **7**, 105.

32 G.-H. Dong, Y.-J. Zhu and L.-D. Chen, *J. Mater. Chem.*, 2010, **20**, 1976.

33 S. Sun, J. Peng, R. Jin, S. Song, P. Zhu and Y. Xing, *J. Alloys Compd.*, 2013, **558**, 6.

34 M. Saleemi, A. Ruditskiy, M. S. Toprak, M. Stingaciu, M. Johnsson, I. Kretzschmar, A. Jacquot, M. Jägle and M. Muhammed, *J. Electron. Mater.*, 2014, **43**, 1927.

35 U. Nithianantham, S. R. Ede, M. Fevzi Ozaydin, H. Liang, A. Rathishkumar and S. Kundu, *RSC Adv.*, 2015, **5**, 89621.

36 G. Thankamma and A. G. Kunjomana, *J. Cryst. Growth*, 2015, **415**, 65.

37 H. Q. Yang, L. Miao, C. Y. Liu, X. Y. Wang, Y. Peng, A. J. Zhang, X. Y. Zhou, G. Y. Wang, C. Li and R. Huang, *Dalton Trans.*, 2016, **45**, 7483.

38 (a) H. J. Breunig and H. Jawad, *Z. Naturforsch., B: Anorg. Chem. Org. Chem.*, 1982, **37**, 1104; (b) S. Heimann, S. Schulz, D. Bläser and C. Wölper, *Eur. J. Inorg. Chem.*, 2013, **28**, 4909.

39 (a) E. R. Parnham and R. E. Morris, *Chem. Mater.*, 2006, **18**, 4882; (b) J. M. Obliosca, S. D. Arco and M. H. Huang, *J. Fluoresc.*, 2007, **17**, 613; (c) N. H. Khan, S. Agrawal, R. I. Kureshy, S. H. R. Abdi, A. Sadhukhan, R. S. Pillai and H. C. Bajaj, *Catal. Commun.*, 2010, **11**, 907.

40 A. S. Pashinkin, A. S. Malkova and M. S. Mikhailova, *Russ. J. Phys. Chem. A*, 2008, **82**, 878.

